



City Research Online

City St George's, University of London

Citation: Yag, Y. & Fu, F. (2022). Axial compressive behaviour of rectangular DCFST stub columns. *Journal of Constructional Steel Research*, 199, 107592. doi: 10.1016/j.jcsr.2022.107592

This is the accepted version of the paper.

This version of the publication may differ from the final published version. To cite this item please consult the publisher's version.

Permanent repository link: <https://openaccess.city.ac.uk/id/eprint/28880/>

Link to published version: <https://doi.org/10.1016/j.jcsr.2022.107592>

Copyright and Reuse: Copyright and Moral Rights remain with the author(s) and/or copyright holders. Copies of full items can be used for personal research or study, educational, or not-for-profit purposes without prior permission or charge, unless otherwise indicated, provided that the authors, title and full bibliographic details are credited, a hyperlink and/or URL is given for the original metadata page and the content is not changed in any way. For full details of reuse please refer to [City Research Online policy](#).

Axial compressive behaviour of rectangular DCFSSST stub columns

You-Fu Yang^{a,*}, Yu-Qin Zhang^a, Feng Fu^b

^a State Key Laboratory of Coastal and Offshore Engineering, Dalian University of Technology, Dalian, 116024, China

^b Department of Engineering, School of Science & Technology, City, University of London, Northampton Square, London, UK

Abstract: In this paper, a new type of rectangular double-opening concrete filled sandwich steel tube (DCFSSST) is developed. This new type of composite section can keep the inner steel tubes away from the cross-sectional centroid axis through the reasonable configuration. In order to assess the structural behaviour of rectangular DCFSSST members, a pilot research on stub columns under axial compression was conducted. A total of 10 specimens, including 5 with double steel square hollow sections (SHSs) and 5 with double steel circular hollow sections (CHSs), were tested with the various offset rate of inner tube (e_0) and opening ratio (ϕ). The experimental observations indicate that, generally, e_0 and ϕ have moderate effect on the failure process and failure modes of the specimens, and the failure modes of the specimens include outward local buckling of outer tube, crushing of the sandwiched concrete and inward local buckling of inner tubes. In addition, ϕ has significant influence on the load-deformation curves, axial capacity and axial compressive stiffness of the specimens; however, e_0 has no obvious effect on the above performance. Moreover, nonlinear finite element (FE) simulation on the behaviour of axially compressed rectangular DCFSSST stub columns was carried out using the ABAQUS software, and the typical performance of new composite members was further analyzed by the verified FE model. Finally, the formulae to calculate the axial capacity of rectangular DCFSSST stub columns were also developed based on the FE simulation results and test results.

Key Words: DCFSSST stub columns; Rectangular section; Axial compression; Tests; FE model; Simplified formulae

*Corresponding author. Tel.: 86-411-8470 8510; Fax: 86-411-8467 4141.

E-mail address: youfuyang@163.com (Dr. You-Fu Yang).

30 **1. Introduction**

31 Concrete filled double-skin steel tube (CFDST) is manufactured by replacing the concrete near the
32 centroid axis of cross section of traditional concrete filled steel tube (CFST) with a steel tube, and in
33 addition to the advantages over the traditional CFST in the structural performance, the CFDST also
34 has the characteristics of more extended cross-section, larger flexural stiffness, lighter self-weight
35 and better seismic performance [1, 2]. As a result, the CFDSTs have potential applications in
36 buildings, bridges and marine structures. However, for the members or structures that need to be
37 porous functionally, withstand heavy loads, and require high stiffness and stability concurrently, such
38 as the giant columns for super high-rise building, the tower columns of bridge or space structure, the
39 piers in a deep valley or the deep sea, and the subsea tunnel or deep sea suspension tunnel, traditional
40 CFST and CFDST members cannot be used or can only be used after considering complex structural
41 measures [3-5].

42 In view of the abovementioned situation, on the basis of traditional rectangular CFDST with both
43 inner and outer tube of steel rectangular hollow section (RHS) [6-11], a new type of composite
44 member, rectangular double-opening concrete filled sandwich steel tube (DCFSST), composed of an
45 outer steel RHS, two symmetrically distributed inner steel square hollow sections (SHSs)/circular
46 hollow sections (CHSs) and the concrete between them, is proposed in this paper. Typical
47 configuration of rectangular DCFSST members is demonstrated in Fig. 1. Compared with the
48 rectangular CFDST, the inner tubes of the rectangular DCFSST are further away from the cross-
49 sectional centroid axis, which results in a larger bending resistance. Simultaneously, replacing one
50 larger inner tube with two smaller ones to form a rectangular DCFSST member has the effect of
51 'breaking up the whole into parts', and thus reducing the cost of transportation, processing and
52 construction of the inner tubes. Furthermore, the sizes and position of both inner tubes can be adjusted
53 to meet different stress conditions while the outer steel RHS kept invariant. For example, the sizes of
54 the inner tube in the tension zone can be increased while the sizes of the inner tube in the compression
55 zone can be reduced simultaneously when the member is mainly subjected to flexural loading.

56 Currently, the structural behaviour of rectangular CFST members have been comprehensively
57 studied by worldwide research organizations [12-14], and the design approaches have also been given
58 in the relevant regulations, e.g. EN 1994-1-1 [15], ANSI/AISC 360-16 [16] and GB/T 51446-2021
59 [17]. At the same time, experimental study and numerical simulation on static property of rectangular
60 CFDST (containing section with outer stainless-steel tube) short members, beams and slender
61 members were performed by a few researchers [6-11], and the corresponding approaches for axial
62 capacity calculation were also proposed [6, 10, 11]. The results showed that, the void ratio of CFDST
63 was an important parameter to be considered in the experiment, and reasonable simplified formulae
64 for axial capacity calculation of CFDST members could be obtained based on the method for
65 traditional CFST considering of the influence of the void ratio. Moreover, Guo et al. [18] carried out
66 tests on the performance of square CFST stub columns with two inner small size steel SHSs/CHSs,
67 and developed the formulae for strength calculation of this kind of composite members.

68 According to above description, it is noticeable that the study on the structural performance of the
69 rectangular DCFSSST members is still rare, which indicates that a fundamental investigation is needed
70 in this area to provide reference for further research and engineering application. As a result, this
71 paper attempts to primarily study the static performance of the rectangular DCFSSST stub columns
72 subjected to axial compression, which can become the basis for the investigation into the performance
73 of this new type of composite members under flexure and compression-flexure. The main purpose of
74 the research includes three aspects: first, to present experimental results of 10 axially compressed
75 rectangular DCFSSST stub columns with various cross-section of inner tubes, offset rate of inner tube
76 and opening ratio; then, to numerically simulate the axial compressive behaviour of the rectangular
77 DCFSSST stub columns and further reveal the failure mechanism of such a kind of composite
78 members; and finally, to propose the simplified formulae for axial capacity calculation of the
79 rectangular DCFSSST stub columns under axial compression.

80 **2. Experimental investigation**

81 **2.1. Details of the specimens**

82 Ten rectangular DCFSSST stub columns, containing 5 specimens with double steel SHSs and 5
83 specimens with double steel CHSs, were prepared to conduct axial compressive tests, and two inner
84 tubes in one specimen were of the same sizes. The cross-sectional dimensions of the specimens are
85 demonstrated in Fig. 2, where, D_o and B_o are overall depth and breadth of outer steel RHS
86 respectively, D_i is overall width or diameter of inner steel SHS or CHS respectively, t_o and t_i are
87 wall thickness of the tubes, and d_e is distance between the centroid of two inner steel tubes about
88 the major axis of section. Moreover, the height (H) to breadth (B_o) ratio of all specimens was identical
89 and set to be 4.0.

90 The experiment was mainly aimed to investigate the influence of two parameters, namely offset
91 rate of inner tube (e_o) and opening ratio (ϕ), and the definition of them is as follows:

$$92 \quad e_o = \frac{d_e}{D_o} \quad (1)$$

$$93 \quad \phi = \sqrt{\frac{\sum_{i=1}^2 A_{si,i}}{A_{ce}}} = \begin{cases} \sqrt{\frac{2B_i^2}{[(D_o-2t_o)(B_o-2t_o)]}} & \text{(with double steel SHSs)} \\ \sqrt{\frac{1.57B_i^2}{[(D_o-2t_o)(B_o-2t_o)]}} & \text{(with double steel CHSs)} \end{cases} \quad (2)$$

94 where, $A_{si,i}$ is the cross-sectional area of the i th inner steel tube, and A_{ce} is the cross-sectional area
95 enclosed by the internal wall of the outer steel RHS.

96 The information of the test specimens is listed in Table 1, in which $N_{u,e}$ and $N_{u,fe}$ are the
97 experimental axial capacity and the simulated axial capacity by finite element (FE) model described
98 later respectively, and K_e is axial compression stiffness of the specimens.

99 The outer steel RHS was manufactured by the cold form processing of the plate and had one straight
100 butt weld, whilst the inner tubes were cut from the finished cold-formed steel SHS or CHS. Each
101 specimen had two endplates with side lengths slightly larger than those of the outer tube and thickness
102 of 20 mm. Before casting the concrete, the first endplate was simultaneously welded to the end of
103 outer and inner tubes using fillet weld, and the welding of the second endplate was conducted after
104 curing the sandwiched concrete for 14 days. It should be noted that, to ensure reliable connection
105 between the inner tubes and the second endplate, two holes with the same cross-section as the inner

106 tubes were drilled at the position of the inner tubes, and a groove for peripheral fillet weld was made
107 in advance at the opening of the endplate. Moreover, eight stiffeners were arranged between each
108 endplate and the external wall of the outer tube to avoid the end damage of the specimens during the
109 loading process.

110 **2.2. Material properties**

111 The properties of each type of steel tube were acquired through axial tension testing of three standard
112 plate coupons. The coupons along the length direction of steel RHS/SHS were taken from the flat
113 portion, while the coupons along the length direction of steel CHS were selected randomly. Table 2
114 presents the measured properties of steel sections, in which, f_y and f_u are the yield and tensile
115 strength, E_s and μ_s are the elastic modulus and Poisson's ratio, and δ is the elongation after
116 fracture.

117 The design strength grade of the sandwiched concrete was C40 (i.e. standard cubic compressive
118 strength of 40 MPa). The materials for producing concrete included: ordinary Portland cement (P.O
119 42.5), fly ash (Grade I), coarse aggregate having particle size between 5 mm and 10 mm, river sand
120 and polycarboxylic acid series of high-performance water reducer. Table 3 presents the mix
121 proportion and properties of the concrete, in which, $f_{cu,28}$ and f_{cu} are the average compressive
122 strength at 28 days and during the test of composite columns obtained by the compression tests on
123 the cubes with a side length of 150 mm, and E_c is the elastic modulus acquired by the compression
124 tests on the prisms with side lengths of 150 mm, 150 mm and 300 mm.

125 **2.3. Test set-up and measuring point arrangement**

126 Static loading tests of the rectangular DCFSSST stub columns were carried out by a testing machine
127 with capacity of 10000 kN. During the test, the specimen was vertically placed on the lower platen,
128 and a load cell was placed between specimen's top endplate and the upper platen to record the applied
129 loads. The overall axial displacements of the specimens were measured by four displacement
130 transducers (DTs) symmetrically placed on the lower platen. The strains at specific points on the steel
131 tubes of the specimens were measured by the strain gauges (SGs) affixed to the external wall of the

132 steel tubes at the half-height section, and there were 24 and 20 SGs for the specimens with double
133 steel SHSs and CHSs, respectively. The test set-up and measuring point arrangement are displayed
134 in Fig. 3.

135 The displacement control approach was used to continuously apply axial compressive loads to the
136 specimens. In the load rising phase, the increasing rate of axial displacement was 0.2 mm/min, while
137 in the load descending stage until the end of the test, the increasing rate of axial displacement was 1.0
138 mm/min. [Simultaneously, a camera facing the half-height on one side of the specimen was used to](#)
139 [record the experimental phenomena and failure process.](#) The test was terminated until the load acting
140 on the specimens fell to 60% of its peak value.

141 **2.4. Experimental results and discussion**

142 **2.4.1. Overall behaviour and failure modes**

143 Careful observation of [the complete video files recorded by the camera](#) indicated that, generally, no
144 obvious change was found in the appearance of all specimens before achieving about 75% peak load,
145 while slight local buckling of outer steel RHS first appeared on the depth side after reaching about
146 75% peak load. Moreover, when the peak load was reached, the first local buckling of outer steel
147 RHS became more obvious and the breadth side of outer steel RHS also buckled locally, accompanied
148 by the sound of concrete crushing. Whereafter, as the axial displacement continued to increase (i.e.
149 damage was intensified), the load on the specimen declined rapidly and became stable gradually.
150 Meanwhile, the local buckling of outer steel RHS became more and more serious together with the
151 possibility of new local buckling, and eventually the main local buckling at four walls and corners of
152 outer steel RHS were connected to form a complete elliptical ring.

153 Fig. 4 demonstrates the overall failure mode of the specimens, where the outward local buckling
154 on front depth side of the outer tube is marked by the continuous dashed lines. It can be seen that,
155 generally, the range and magnitude of local buckling of the tube depth side are larger than those of
156 the tube breadth side as the depth side of the outer steel RHS has a higher width-to-thickness ratio,
157 and each specimen possesses a connection of primary local buckling on four sides and corners of the

158 outer tube. At the same time, the range and magnitude of subsequent local buckling (if any) of the
159 outer tube are weaker than those of primary local buckling, and usually cannot form the four-sided
160 connectivity. These failure characteristics are similar to those of previous tests [6-8]. In general, the
161 influence of offset rate of inner tube (e_0) and opening ratio (ϕ) on the overall failure mode of the
162 specimens is not evident, and the difference in the buckling form of the outer tube is mainly caused
163 by the material defects and fabrication deviation of the specimens.

164 The failure mode of the sandwiched concrete is shown in Fig. 5. It can be seen that, in general, the
165 failure characteristics of the concrete is similar regardless of the parameters of the specimens. The
166 sandwiched concrete is crushed and separated from its main body within local buckling area of the
167 outer tube, and simultaneously the sandwiched concrete has no obvious damage outside the local
168 buckling area of the outer tube.

169 Fig. 6 exhibits the failure mode of the inner tubes after completion of the tests. It can be seen that,
170 generally, the inward local buckling around the half-height section of the specimens occurs in both
171 tubes, as the possible outward local buckling of the inner tubes was stopped by the sandwiched
172 concrete. For the rectangular DCFSSST specimens with double steel SHSs, there are serious folding-
173 shaped local buckling on all side walls of the inner tubes, which extends to the four corners of each
174 tube. However, for the rectangular DCFSSST specimens with double steel CHSs, the inward necked
175 local buckling of the inner tubes generally perpendicular to the major axis of the cross-section is
176 formed as the outer tube breadth side with a smaller width-to-thickness ratio leads to a stronger
177 constraint to the sandwiched concrete, i.e. resulting in a greater lateral stresses of the sandwiched
178 concrete on the inner tubes along major axis of the cross-section. Moreover, the offset rate of inner
179 tube (e_0) and opening ratio (ϕ) have no obvious effect on the buckling form and position of the inner
180 tubes.

181 **2.4.2. Load versus displacement curves**

182 The obtained load (N) versus axial displacement (Δ) curves are displayed in Fig. 7 by the solid lines.
183 It can be observed that, regardless of the difference in the experimental parameters, the $N - \Delta$ curve

184 of all specimens generally includes four stages of approximate elastic, elastic-plastic, rapid decline
185 from the peak and final stable stage. However, compared with the specimens with double steel CHSs,
186 the specimens with double steel SHSs have a faster load decline rate from the peak and a lower
187 residual capacity at the final stable stage. This is mainly because the D_i/t_i of inner steel SHSs is
188 larger than that of inner steel CHSs, causing a lesser post-buckling capacity. Overall, the slope of
189 approximate elastic and prophase of elastic-plastic stage on the $N - \Delta$ curves changes with the
190 variation in the material and geometric parameters. However, the slope of the $N - \Delta$ curve before
191 reaching the peak generally decreases with the increase of opening ratio (ϕ). This can be explained
192 that, while ϕ is increased, the load carrying capacity increase caused by tube area increase is lower
193 than the axial capacity decrease caused by the concrete area reduce. The peak load on the $N - \Delta$
194 curve is determined as axial capacity of the specimens (N_{ue}), which are summarized in Table 1.

195 **2.4.3. Load versus strain relationship**

196 From the start of loading until the N_{ue} is reached, typical longitudinal strain distribution of the
197 specimens is schematically displayed in Fig. 8, where n ($=N/N_{ue}$) is the load level, and for the outer
198 steel RHS and inner steel SHS, the strain of the remaining locations without SG is determined by that
199 of axisymmetric measuring points about the centroid axis, while for the inner steel CHS, the strain of
200 locations without SG is determined by the linear interpolation of strain at measuring points according
201 to their arc length from the measuring points. It should be noted that, the strain distribution after
202 reaching N_{ue} is not included as local buckling position of the outer steel RHS is not completely
203 located at the half-height section, thus producing an irregular strain distribution. It is shown that,
204 generally, when $n \leq 0.5$, the longitudinal strain of all steel tubes increases almost proportionally,
205 and the strain reading of all measuring points is close, indicating that the specimen is basically in the
206 elastic state. However, when $n > 0.5$, the strain increasing rate at each point improves significantly;
207 however, the strain distribution is asymmetrical because of the asymmetry of the outer tube buckling
208 position. Simultaneously, the steel RHS and SHS show a trend that the strain at the corner portion is
209 larger than that at the side middle, that is, the load is transferred from the side middle to the corner of

210 the steel tube after local buckling occurred, and the strain difference between corner portion and side
211 middle increases with the increase of n , while the strain of the inner steel CHS increases almost
212 uniformly during the loading process. In addition, the strain development of the inner steel CHS is
213 more uniform and sufficient than that of the inner steel SHS.

214 The load (N) versus strain (ε) curves of typical specimens is demonstrated in Fig. 9, where the
215 strain at all symmetric positions is averaged to one value, the tensile and compressive strains are
216 respectively treated as positive and negative, and ε_y is the average yield strain of the outer and inner
217 tubes in one specimen. It is shown that, the variation trend of $N - \varepsilon$ curves at all measuring points
218 are generally similar, but the strain values under the same load level are different. In general, the
219 strain at the corner portion is larger than that at the side middle, and the strain at the breadth corner is
220 larger than that at the depth corner, indicating that the constraint of the outer steel RHS on the
221 sandwiched concrete mainly concentrates on the breadth corner of the cross-section. It can also be
222 observed that, the conformity between local buckling position of the steel tubes and the half-height
223 section of the specimens directly determines the strain development after reaching N_{ue} . For example,
224 the local buckling of the outer steel RHS and inner steel SHS of specimen S0.40-57 is almost located
225 at the half-height section, resulting in a more adequate strain development in the post-peak stage;
226 however, the local buckling of the outer steel RHS and inner steel CHS of specimen C0.35-48 has
227 certain deviation from the half-height section, leading to a relatively deficient strain development
228 during the post-peak stage. In addition, when the N_{ue} is achieved, the longitudinal strain of each
229 measuring point is higher than ε_y , that is, the half-height section of all steel tubes can attain its yield
230 state.

231 Fig. 10 shows the effect of parameters on the measured load (N) versus longitudinal strain (ε_L)
232 curves at representative points (a, b and e) by solid lines. It can be observed that, generally, the
233 influence of the type of inner tubes, e_0 and ϕ on the elastic stage of $N - \varepsilon_L$ curve is not obvious.
234 In the elastic-plastic stage, e_0 has no evident effect on the $N - \varepsilon_L$ curve, whilst ϕ has a significant
235 effect on the $N - \varepsilon_L$ curve, namely ε_L increases with the increase of ϕ under the same load level.

236 This is mainly due to the fact that, the variation in e_0 only changes the distribution of materials
 237 within the cross-section and does not fundamentally change the cross-sectional characteristics. At the
 238 same time, while ϕ increased, the area of the sandwiched concrete reduces, which weakens its
 239 supporting effect on the local buckling of the outer and inner steel tubes, leading to a earlier local
 240 buckling of them. Moreover, under different parameters, there is a remarkable difference in the post-
 241 peak phase of $N - \varepsilon_L$ curve, which is mainly caused by the discrepancy between the local buckling
 242 (failure) positions of the steel tubes and the location (half-height section) of the strain gauges.

243 **2.4.4. Mechanical indicators**

244 To investigate the relationship between the axial capacity of the specimens and their sectional strength,
 245 the axial capacity factor (F_b) is defined as follows:

$$246 \quad F_b = \frac{N_{u,e}}{N_{uso} + N_{uc} + N_{usi}} \quad (3)$$

247 where, $N_{uso}(=f_{yo}A_{so})$, $N_{uc}(=f'_c A_c)$ and $N_{usi}(=\sum f_{yi,i}A_{si,i})$ are the sectional strength of the outer
 248 steel tube, the sandwiched concrete and the inner steel tubes, respectively, f_{yo} , f'_c and $f_{yi,i}$ are the
 249 yield strength of the outer steel tube, the cylindrical compressive strength of concrete and the yield
 250 strength of the i th inner steel tube, respectively, and A_{so} and A_c are the cross-sectional area of the
 251 outer steel tube and the sandwiched concrete, respectively. [In this paper, the provisions in the EN](#)
 252 [1992-1-1 \[19\] were used to convert \$f_{cu}\$ to \$f'_c\$.](#)

253 The effect of parameters (e_0 and ϕ) on $N_{u,e}$ and F_b of the specimens is indicated in Fig. 11(a).
 254 The results show that, F_b is generally larger than 1.0 and the average value of F_b of specimens with
 255 double steel SHSs and those with double steel CHSs equal to 1.058 and 1.024, respectively, which
 256 indicates that the steel RHS with $D_o/B_o = 2.0$ still has constraint effect on the sandwiched concrete
 257 while the inner tubes provide reliable support. It can also be observed that, generally, a higher ϕ
 258 leads to a smaller $N_{u,e}(F_b)$, considering that the decrease of the concrete area has a more obvious
 259 effect on the reduction of axial capacity. However, there is no consistent effect of e_0 on $N_{u,e}(F_b)$ of
 260 the two types of specimens, as the inner tubes of the specimens generally exhibit failure by reaching
 261 the yield state, which is independent of their positions.

262 Referring to the approach in Yang et al. (2021) [20], axial compression stiffness (K_e) of the
263 rectangular DCFSSST stub columns is defined as follows:

$$264 \quad K_e = \frac{0.4N_{u,e}}{\varepsilon_{L,0.4}} \quad (4)$$

265 where, $\varepsilon_{L,0.4}$ is the average longitudinal strain when the load in the ascending phase of the measured
266 $N - \varepsilon_L$ curve reaches $0.4N_{u,e}$.

267 Simultaneously, axial compression stiffness ratio (R_k) is further defined to discover the
268 relationship between K_e of the specimens and their sectional compressive stiffness:

$$269 \quad R_k = \frac{K_e}{E_{s0}A_{s0} + E_cA_c + \sum E_{si,i}A_{si,i}} \quad (5)$$

270 where, E_{s0} , E_c and $E_{si,i}$ are the elastic modulus of outer steel tube, the sandwiched concrete and
271 the i th inner steel tube, respectively.

272 Fig. 11(b) demonstrates the influence of e_0 and ϕ on $K_e(R_k)$ of the specimens. It is shown that,
273 K_e and R_k of two types of specimens exhibit the same variation trend when the experimental
274 parameters change, i.e., $K_e(R_k)$ generally decreases with the increase of ϕ and e_0 has no
275 consistent influence on $K_e(R_k)$. These are similar to the trend in Fig. 11 (a). Moreover, R_k has a
276 mean and standard deviation (SD) of 0.923 and 0.039, respectively. This means that, the axial
277 compression stiffness (K_e) of rectangular DCFSSST stub columns can be calculated based on the
278 elastic modulus and area of each component, and generally the safe calculation results can be obtained.

279 **3. Finite element (FE) simulation**

280 **3.1. General description**

281 To better theoretically understand the axial compressive behaviour of the rectangular DCFSSST stub
282 columns, nonlinear finite element (FE) models were constructed by software ABAQUS [21].

283 The elastic properties of the steel tubes, including E_s and μ_s , replicated those obtained from
284 tensile coupon tests (see Table 2). The inelastic property of the steel tubes, i.e. the relationship
285 between true stress and plastic strain, was depicted using the metal plasticity model in the software
286 [21]. As stated earlier, the outer steel RHS and inner steel SHSs of the specimens were cold-formed,

287 which means that their flat and corner portion have different material properties. Therefore, the
 288 relationship between true stress and plastic strain of the flat portion in the steel RHS and SHSs was
 289 acquired by transforming the engineering stress (σ_s) versus engineering strain (ε_s) relationship in [22],
 290 as indicated in Eq. (6a). At the same time, the $\sigma_s - \varepsilon_s$ relationship of corner portion of the steel RHS
 291 and SHSs was same as that of flat portion; however, a higher yield strength for the corner portion was
 292 determined according to the ratio of corner radius to thickness and the ratio of tensile strength to yield
 293 strength of flat portion [22]. In the FE modelling, the approach for determining the weighted-average
 294 yield strength and the corner radius of the cold-formed steel RHS as well as SHSs in [23] and [24]
 295 was employed, respectively. In addition, for the inner steel CHSs, the true stress versus plastic strain
 296 relationship was acquired by transforming the $\sigma_s - \varepsilon_s$ relationship including five segments in [20],
 297 as indicated in Eq. (6b). In order to simplify the numerical simulation reasonably and ensure its
 298 convergence, both endplates of the specimens were ignored, and the boundary conditions were
 299 applied to the same plane of steel tubes and the sandwiched concrete.

$$300 \quad \sigma_s = \begin{cases} E_s \varepsilon_s & (\varepsilon_s \leq \varepsilon_a) \\ f_p + E_{s1}(\varepsilon - \varepsilon_e) & (\varepsilon_a < \varepsilon_s \leq \varepsilon_b) \\ f_{ym} + E_{s2}(\varepsilon - \varepsilon_{e1}) & (\varepsilon_b < \varepsilon_s \leq \varepsilon_c) \\ f_y + E_{s3}(\varepsilon - \varepsilon_{e1}) & (\varepsilon_s > \varepsilon_c) \end{cases} \quad (6a)$$

301 where, $f_p = 0.75f_y$, $f_{ym} = 0.875f_y$, $E_{s1} = E_s/2$, $E_{s2} = E_s/10$, $E_{s3} = E_s/200$, $\varepsilon_a = 0.75f_y/E_s$,
 302 $\varepsilon_b = \varepsilon_a + 0.125f_y/E_{s1}$, and $\varepsilon_c = \varepsilon_b + 0.125f_y/E_{s2}$.

$$303 \quad \sigma_s = \begin{cases} E_s \varepsilon_s & (\varepsilon_s \leq \varepsilon_e) \\ -A\varepsilon_s^2 + B\varepsilon_s + C & (\varepsilon_e < \varepsilon_s \leq \varepsilon_y) \\ f_y & (\varepsilon_y < \varepsilon_s \leq \varepsilon_n) \\ f_y \left(1 + 0.6 \frac{\varepsilon_s - \varepsilon_n}{\varepsilon_u - \varepsilon_n} \right) & (\varepsilon_n < \varepsilon_s \leq \varepsilon_u) \\ 1.6f_y & (\varepsilon_s > \varepsilon_u) \end{cases} \quad (6b)$$

304 where, $\varepsilon_e = 0.8 f_y/E_s$, $\varepsilon_y = 1.5\varepsilon_e$, $\varepsilon_n = 10\varepsilon_y$, $\varepsilon_u = 100\varepsilon_y$, $A = 0.2 f_y/(\varepsilon_y - \varepsilon_e)^2$, $B = 2A\varepsilon_y$, and $C =$
 305 $0.8f_y + A\varepsilon_e^2 - B\varepsilon_e$.

306 The elastic properties of the sandwiched concrete, including elasticity modulus and Poisson's ratio,
 307 were set to be $4730\sqrt{f'_c}$ [25] and 0.2 [26], respectively. The damaged plasticity model in the
 308 software [21] was employed to capture the inelasticity of the sandwiched concrete, in which, the

309 isotropic compressive/tensile plasticity and isotropic damaged elasticity were assumed, and the yield
310 and failure surface were controlled by the equivalent compressive/tensile plastic strain. The tension
311 stiffening of the sandwiched concrete was captured through the fracture energy cracking criterion
312 [21]. Moreover, it is noted that, the D_i/t_i of the inner steel tubes in the rectangular DCFSSST stub
313 column specimens is lower than the limit of hollow steel tube in steel structures, and the experimental
314 results also show that the inner steel tubes can provide reliable support for the sandwiched concrete
315 until the axial capacity is reached, that is, the structural properties of the sandwiched concrete are
316 consistent with the concrete core of the corresponding rectangular CFST and CFDST stub columns
317 [6, 10, 12], i.e. the confinement effect of the outer steel RHS on the sandwiched concrete needs to be
318 incorporated. As a result, the engineering stress (σ_c) versus engineering strain (ε_c) relationship under
319 compression in [12, 27] was chosen to get the input data pair between compressive stress and inelastic
320 strain of the sandwiched concrete in the rectangular DCFSSST stub columns, as described in the
321 following equations:

$$322 \quad \sigma_c/f'_c = \begin{cases} 2(\varepsilon_c/\varepsilon_{c0}) - (\varepsilon_c/\varepsilon_{c0})^2 & (\varepsilon_c/\varepsilon_{c0} \leq 1) \\ \frac{\varepsilon_c/\varepsilon_{c0}}{\rho \cdot (\varepsilon_c/\varepsilon_{c0} - 1)^m + \varepsilon_c/\varepsilon_{c0}} & (\varepsilon_c/\varepsilon_{c0} > 1) \end{cases} \quad (7)$$

323 where, $\varepsilon_{c0} = (1300 + 12.5f'_c + 800\xi^{0.2})/1E6$, $\rho = (f'_c)^{0.1}/(1.2\sqrt{1 + \xi})$, $m = 1.5(\varepsilon_{c0}/\varepsilon_c) +$
324 1.6, and ξ is the nominal confinement factor [6].

325 All steel tubes were modelled by S4 elements having 9 integration points along the thickness, and
326 the sandwiched concrete was simulated by C3D8R elements. In the modelling, the steel tubes and the
327 sandwiched concrete possessed the same meshing nodes to ensure connectivity and computational
328 efficiency. The surface-to-surface contacts were defined to reproduce the interfacial properties
329 between steel tubes and the sandwiched concrete of the rectangular DCFSSST stub columns. The ‘hard
330 contact’ was considered in the normal direction, and the ‘Coulomb friction’ model with the friction
331 coefficient of 0.6 [12, 28] was adopted in the tangential directions. Fig. 12 shows the meshing of the
332 FE model.

333 During the FE modelling, the boundary conditions of the rectangular DCFSSST stub columns
334 subjected to axial compression are also shown in Fig. 12. In the initial step, the ‘ENCASTRE’ was

335 defined as the boundary conditions of the bottom plane, that is, all degrees of freedom were restricted,
336 and for the top plane the ' $U_x=U_y=0$ ' was defined, i.e. translational displacements in both directions
337 were prevented. In the loading step, axial displacements of 40 mm were acted upon the top plane. It
338 is noted that, for the axially compressed rectangular DCFSSST stub columns, the residual stresses
339 together with initial imperfections of steel RHS/SHSs are not included in the FE modelling according
340 to the research outcomes presented in [28].

341 **3.2. Validation of the FE model**

342 Fig. 13 demonstrates the modelled failure modes of different components in typical rectangular
343 DCFSSST stub column specimens. It is shown that, generally, the simulated failure mode of the
344 outward local buckling of the outer steel RHS (Fig. 13(a)) and the inward local buckling of the inner
345 steel tubes (Fig. 13(c)) accords well with the experimental results (Figs. 4 and 6); however, the
346 simulated local buckling position (around half-height section) differ from the tested one, to some
347 extent. This is mainly because the actual conditions of the test specimens, such as the random
348 distribution of material defects in each component, local size deviation and eccentricity of loading,
349 cannot be effectively considered by the FE model. In addition, the results in Figs. 5 and 13(b) indicate
350 that, both the simulated and measured failure mode of the sandwiched concrete occur in the local
351 buckling position(s) of the steel tubes.

352 The comparison of load (N) versus deformation (Δ and ε) curves between the predicted and
353 measured results is demonstrated in Figs. 7 and 10, where the capital letters P and M in parentheses
354 following the specimen label represent the predicted and measured curve, respectively. It is shown
355 that, with the increase of the deformations, the variation trend of the simulated load is generally
356 consistent with that of the measured one; however, there is a certain deviation between the simulated
357 curve and the corresponding one from the tests, including a higher slope before reaching N_{ue} and a
358 lower slope after reaching N_{ue} of the simulated curves. This can also be explained that, the current
359 FE model cannot reasonably consider the real conditions of the specimens mentioned above.

360 Fig. 14 shows the comparison between the simulated axial capacities using the FE model ($N_{u,fe}$)

361 and the measured axial capacities ($N_{u,e}$) of the axially compressed rectangular DCFSSST stub column
362 specimens in this study. The results indicate that the overall difference between $N_{u,fe}$ and $N_{u,e}$ is
363 within 10%, and the mean and SD of $N_{u,fe}/N_{u,e}$ equal to 0.960 and 0.038, respectively. It can be
364 found that the FE model built in this paper can better predict the axial capacity of the rectangular
365 DCFSSST stub columns under axial compression.

366 3.3. Analysis using the FE model

367 Based on the above FE model verified by the experimental observations, the axial compressive
368 behaviour of the rectangular DCFSSST stub columns is further analyzed with e_0 and ϕ as main
369 parameters. The basic conditions of the example are as follows: $D_o \times B_o = 600 \text{ mm} \times 300 \text{ mm}$,
370 $H = 1200 \text{ mm}$, $D_o/t_o = 54.5$ (i.e. nominal steel ratio $\alpha_n = A_{so}/A_{ce} = 0.11$), $t_i = 4 \text{ mm}$, $f_{yo} =$
371 $f_{yi} = 345 \text{ MPa}$, $f'_c = 50 \text{ MPa}$, $e_0 = 0.5$, and for the columns with double steel SHSs, $\phi = 0.59$,
372 and for the columns with double steel CHSs, $\phi = 0.53$.

373 Fig. 15 shows the computed $N - \varepsilon_L$ curve of typical rectangular DCFSSST stub columns under
374 axial compression, where DS and DC in parentheses represent the columns with double steel SHSs
375 and CHSs, respectively. It can be observed that, generally, the effect of e_0 and ϕ on the calculated
376 $N - \varepsilon_L$ curve is similar to the experimental results, i.e. e_0 has a moderate on the trend of the $N -$
377 ε_L curve and the axial capacity (N_u) of the columns; however, the columns with a smaller ϕ have a
378 larger N_u and a higher post-peak strength. It should be noted that, the capacity of column having
379 double steel SHSs and $\phi = 0.82$ ($B_i/t_i = 58$) continued to decrease after the peak, indicating that
380 the inner steel SHSs could not provide a stable capacity after locally buckling. Therefore, for the
381 rectangular DCFSSST columns, the attention should be paid to the matching of ϕ with B_i/t_i of the
382 inner steel SHSs in practical design.

383 The effect of ϕ on stress state of different components in the axially compressed rectangular
384 DCFSSST stub columns while reaching the axial capacity (N_u) is demonstrated in Fig. 16, and the
385 results for e_0 change are not shown as its influence is moderate. It can be observed that, generally,
386 ϕ has no obvious impact on the Mises stress distribution and values of the steel tubes, that is, the

387 Mises stress of flat and corner portion in the outer steel RHS as well as the inner steel SHSs reaches
388 their yield strength, and the Mises stress of the inner steel CHSs also reaches their yield strength.
389 Moreover, the longitudinal stresses (S_{33}) across the section of the sandwiched concrete reach its
390 maximum in the corner and gradually decays to the side middle, and the maximum stress is obviously
391 higher than f'_c , which is consistent with the characteristics of rectangular CFST [12]. At the same
392 time, the S_{33} of the sandwiched concrete decreases with the increase of ϕ , especially for the columns
393 with double steel CHSs.

394 The effect of e_0 and ϕ on interaction stress (p) between steel tube and the sandwiched concrete
395 at the representative points is indicated in Fig. 17. It can be seen that, generally, p at the corner of
396 the outer steel RHS (point a) is significantly higher than that at the side middle of the inner steel tubes
397 (points b, d and f), indicating that the constraint effect of the outer tube on the concrete is obviously
398 stronger than the supporting effect of the inner tubes. This is consistent with the S_{33} distribution
399 results of the sandwiched concrete in Fig. 16. At point a, the variation of p reflects that the outer
400 tube and concrete are stressed separately at first and contact with each other quickly until the peak
401 attains; however, p decreases first and then increases slowly due to the local buckling of the outer
402 tube. Furthermore, p generally decreases with the increase of e_0 and ϕ , and the effect of ϕ on p
403 is more significant than e_0 as the change of ϕ significantly changes the volume of the sandwiched
404 concrete. At points b, d and f, e_0 and ϕ have no consistent effect on p , which may be caused by
405 the subtle differences in the buckling process and morphology of the inner tubes.

406 **4. Simplified formulae for calculating the axial capacity**

407 By investigating the FE simulation results of the test specimens and the designed examples in Figs.
408 13 and 16, it can be observed that, the inner steel tubes of the rectangular DCFSSST stub columns
409 under axial compression generally reach their yielding state while the axial capacity achieved, which
410 is consistent with the previous findings [6, 20]. As a result, the yield strength of the inner steel tubes
411 can be directly subtracted from the axial capacity of new composite columns to assess the influence

412 of parameters on the strength of the outer tube and the sandwiched concrete, and the strength index
 413 ($f_{scy,d}$) of the rectangular DCFSSST stub columns under axial compression is defined as follows:

$$414 \quad f_{scy,d} = \frac{N_u - \sum f_{yi,i} A_{sh,i}}{(A_{so} + A_c)} \quad (8)$$

415 Furthermore, in view of the fact that the cross-sectional composition of a rectangular DCFSSST is
 416 similar to that of a rectangular CFDST, as well as the similar stress state of the steel tube(s) inside
 417 them while N_u is reached, the strength index ratio (k) of the former and the latter is defined as:

$$418 \quad k = \frac{f_{scy,d}}{f_{scy,s}} \quad (9)$$

419 in which, $f_{scy,s}$ is the simplified strength index of a rectangular CFDST [6].

420 The effect of parameters on the strength index ratio (k) is demonstrated in Fig. 18. It can be seen
 421 that, regardless of the type of inner tubes, the k values are generally maintained around 1.0, although
 422 individual parameters (e.g. $f_{yo(i)}$ and f'_c) have a certain influence on k , that is, the simplified
 423 strength index ratio of the rectangular CFDST can be directly applied to the rectangular DCFSSST.

424 According to Eqs. (8) and (9), the formula for the axial capacity calculation of the rectangular
 425 DCFSSST stub columns can be obtained:

$$426 \quad N_u = [C_1 \phi^2 f_{yo} + C_2 (1.18 + 0.85\xi) f_{ck}] (A_{so} + A_c) + \sum f_{yi,i} A_{sh,i} \quad (10)$$

427 where, C_1 and C_2 are the parameters related to the steel ratio and nominal steel ratio, and f_{ck} is
 428 the characteristic compressive strength of concrete [1, 6].

429 The comparison between the calculation results ($N_{u,s}$) of Eq. (10) and the FE simulation results
 430 ($N_{u,fe}$) as well as experimental results ($N_{u,e}$) is respectively shown in Figs. 19 and 20, and the mean
 431 and SD of $N_{u,s}/N_{u,fe}$ ($N_{u,s}/N_{u,e}$) are 0.997 (0.955) and 0.030 (0.045), respectively. It can be found
 432 that, the calculated axial capacities of the axially compressed rectangular DCFSSST stub columns
 433 using the simplified formulae are in good agreement with the FE simulation and experimental results,
 434 and the differences between the objects of comparison are generally within 10%. [Based on the](#)
 435 [experimental and numerical studies in this paper, the application range of Eq. \(10\) is: \$D_o=300-600\$](#)
 436 [mm, \$\alpha_n=0.06-0.18\$, \$e_o=0.35-0.6\$; \$\phi=35\%-82\%\$, \$f_y=235-460\$ MPa, \$f'_c=25-75\$ MPa, and \$D_i/t_i <\$](#)

437 $[D_i/t_i]$, where $[D_i/t_i]$ is the limit of the width/diameter-to-thickness ratio of the inner steel tubes.

438 **5. Conclusions**

439 The axial compressive behaviour of a new type of rectangular double-opening concrete filled
440 sandwich steel tube (DCFSST) stub column is investigated, and based on the experiments and
441 numerical simulations in this study the following conclusions can be drawn:

442 (1) The observed failure modes of typical specimens show that, offset rate of inner tube (e_0) and
443 opening ratio (ϕ) have a moderate effect on the failure modes of rectangular DCFSST stub column
444 specimens. In general, there are 1 to 2 outward local buckling spots noticed in the various locations
445 on outer steel RHS and the local buckling on the depth side is more obvious than that on the breadth
446 side. Moreover, the sandwiched concrete is crushed at the buckling position of the outer tube, while
447 both inner steel tubes buckle inwards in the crushed location of the sandwiched concrete.

448 (2) The relationship between load (N) and axial displacement (Δ)/strain (ε) of the specimens are
449 recorded, and the results demonstrate that e_0 generally has little effect on the initial slope of $N - \Delta$
450 curve of rectangular DCFSST stub columns; however, the slope of the ascending stage of $N - \Delta$
451 curve decreases with the increase of ϕ , and the deformability of the specimens with double steel
452 CHSs is better than those with double steel SHSs. The variation trend of $N - \varepsilon$ curve is generally
453 consistent with that of $N - \Delta$ curve. Simultaneously, at the half-height section of the outer steel RHS,
454 the strain development of side middle is slower than that of corner portion.

455 (3) The variation characteristics of the key mechanical indexes of the specimens are studied, and it
456 is found that the axial capacity (N_{ue}) and axial compression stiffness (K_e) of the specimens generally
457 decreases while ϕ increased; however, the effect of e_0 on N_{ue} and K_e is not obvious. The axial
458 compression stiffness (K_e) of rectangular DCFSST stub columns can be safely determined by the
459 summation of the product of elastic modulus and area of each component.

460 (4) The finite element (FE) simulation is conducted, and the modelling results indicate that the
461 constructed FE model can well reproduce the failure process and modes, load-deformation curves,
462 axial capacity and stress state of the rectangular DCFSST stub columns under axial compression. In

463 addition, the interaction stress (p) at the corner of the outer steel RHS, which well reflects the change
464 in loading state between outer tube and concrete, is much higher than that at the side middle of the
465 inner steel tubes, and e_0 and ϕ have remarkable effect on p at the corner of the outer steel RHS.

466 (5) A simplified method for axial capacity calculation is suggested, and the comparison shows that
467 the simplified formulae based on the parameter analysis results can accurately predict the axial
468 capacity of DCFSSST stub columns under axial compression, and the difference between the
469 simplified and the FE simulation/measured results is within 10%.

470 It's worth noting that the rectangular DCFSSST members may bear the combined action of axial
471 forces and bending moments. As a result, further studies on the performance of rectangular DCFSSST
472 beams and beam-columns are necessary for guiding their design and application.

473 **Declaration of Competing Interest**

474 The authors declare that they have no known competing financial interests or personal relationships
475 that could have appeared to influence the work reported in this paper.

476 **Acknowledgement:**

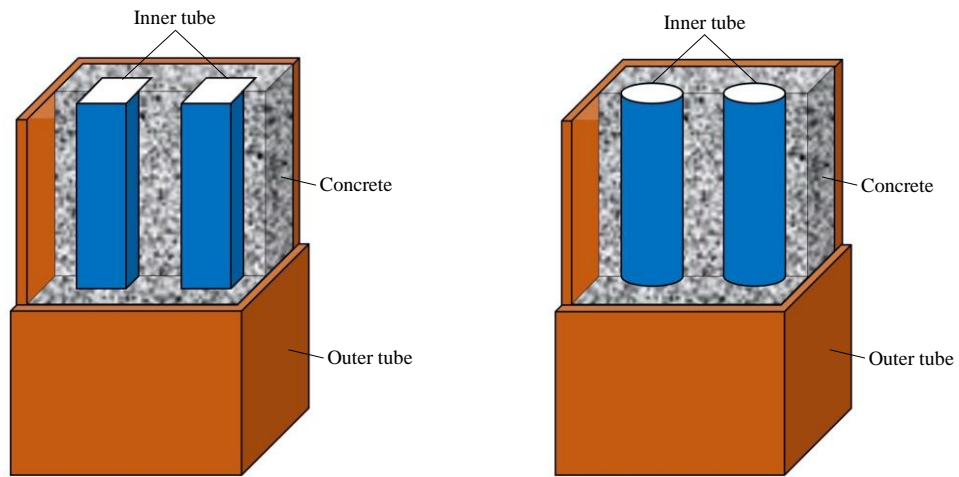
477 The research work reported herein was supported by the National Natural Science Foundation of
478 China (No. 51678105). The research funding is highly appreciated. The authors also wish to thank
479 Ms. Min Hou for her help in the tests.

480 **References:**

- 481 [1] L.H. Han, D. Lam, D.A. Nethercot, Design Guide for Concrete-Filled Double Skin Steel Tubular
482 Structures, CRC Press, UK, 2018.
- 483 [2] L. H. Han, W. Li, R. Bjorhovde, Developments and advanced applications of concrete-filled steel
484 tubular (CFST) structures: Members, J. Constr. Steel. Res. 100 (2014) 211-228.
- 485 [3] M.C.H. Hui, C.K.P. Wong, Stonecutters Bridge-durability, maintenance and safety considerations,
486 Struct. Infrastruct. Eng. 5(3) (2009) 229-243.
- 487 [4] X. Lu, X. Lu, H. Guan, W. Zhang, L. Ye, Earthquake-induced collapse simulation of a super-tall
488 mega-braced frame-core tube building, J. Constr. Steel. Res. 82 (2013) 59-71.
- 489 [5] Z.B. Wang, L.H. Han, W. Li, Z. Tao, Seismic performance of concrete-encased CFST piers:
490 experimental study, J. Bridge Eng. 21(4) (2016) 04015072.
- 491 [6] Z. Tao, L.H. Han, Behaviour of concrete-filled double skin rectangular steel tubular beam-
492 columns, J. Constr. Steel. Res. 62(7) (2006) 631-646.

- 493 [7] L. Xie, M. Chen, H. Huang, Experimental study on rectangular concrete-filled double-skin steel
494 tubes subjected to axial compressive load, *Industrial Construction* 43(5) (2013) 128-131. (in
495 Chinese)
- 496 [8] H. Huang, Y. Zhu, M. Chen, K. Xu, Experimental investigation on axial compression of
497 rectangular recycled concrete-filled double-skin steel tube short column, *J. Experimental*
498 *Mechanics* 31(1) (2016) 67-74. (in Chinese)
- 499 [9] M. Rizwan, Q.Q. Liang, M.N.S. Hadi, Numerical analysis of rectangular double-skin concrete-
500 filled steel tubular slender columns incorporating interaction buckling, *Eng. Struct.* 245 (2021)
501 112960.
- 502 [10] M. Rizwan, Q.Q. Liang, M.N.S. Hadi, Fiber-based computational modeling of rectangular
503 double-skin concrete-filled steel tubular short columns including local buckling, *Eng. Struct.* 248
504 (2021) 113268.
- 505 [11] M. Ahmed, Q.Q. Liang, A. Hamoda, M. Arashpour, Behavior and design of thin-walled double-
506 skin concrete-filled rectangular steel tubular short and slender columns with external stainless-
507 steel tube incorporating local buckling effects, *Thin-Walled Struct.* 170 (2022) 108552.
- 508 [12] Y.F. Yang, C. Hou, M. Liu, Tests and numerical simulation of rectangular RACFST stub columns
509 under concentric compression, *Structures* 27 (2020) 396-410.
- 510 [13] Y.F. Yang, Y.Q. Zhang, F. Fu, Performance and design of RAC-filled steel RHS beams, *J. Build.*
511 *Eng.* 46 (2022) 103734.
- 512 [14] Y. Wang, H. Lin, Z. Lai, D. Li, W. Zhou, X. Yang, Flexural behavior of high-strength rectangular
513 concrete-filled steel tube members, *J. Struct. Eng.* 148(1) (2022) 04021230.
- 514 [15] EN 1994-1-1. Eurocode 4: Design of Composite Steel and Concrete Structures-Part 1-1: General
515 Rules and Rules for Buildings, European Committee for Standardization, Brussels, Belgium,
516 2004.
- 517 [16] ANSI/AISC 360-16. Specification for Structural Steel Buildings, American Institute of Steel
518 Construction (AISC), Chicago, USA, 2016.
- 519 [17] GB/T 51446-2021. Technical Standard for Concrete-Filled Steel Tubular Hybrid Structures,
520 Beijing: China Architecture & Building Press, 2021.
- 521 [18] Z. Guo, Y. Chen, Y. Wang, M. Jiang, Experimental study on square concrete-filled double skin
522 steel tubular short columns, *Thin-Walled Struct.* 156 (2020) 107017.
- 523 [19] EN 1992-1-1. Eurocode 2: Design of Concrete Structures-Part 1-1: General Rules and Rules for
524 Buildings, European Committee for Standardization, Brussels, Belgium, 2004.
- 525 [20] Y.F. Yang, F. Fu, X.M. Bie, X. H. Dai. Axial compressive behaviour of CFDST stub columns
526 with large void ratio, *J. Constr. Steel. Res.* 186 (2021) 106892.
- 527 [21] Simulia, ABAQUS Analysis User's Guide, Version 6.14, Dassault Systèmes Simulia Corp,
528 Providence, RI, 2014.
- 529 [22] N. Abdel-Rahman, K.S. Sivakumaran, Material properties models for analysis of cold-formed
530 steel members, *J. Struct. Eng.* 123(9) (1997) 1135-1143.
- 531 [23] M. Elchalakani, X.L. Zhao, R. Grzebieta, Tests on concrete filled double-skin (CHS outer and
532 SHS inner) composite short columns under axial compression, *Thin-Walled Struct.* 40 (5) (2002)
533 415-441.

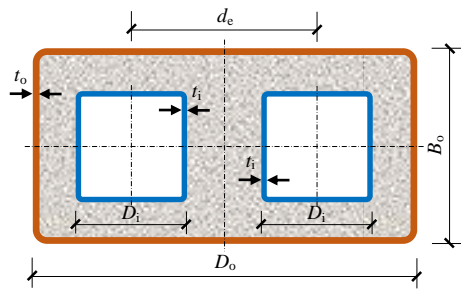
- 534 [24] AISI, North American Specification for the Design of Cold-formed Steel Structural Members,
535 American Iron and Steel Institute (AISI), North American Standard, Washington DC, USA, 2001.
- 536 [25] ACI Committee 318, Building Code Requirements for Structural Concrete (ACI 318-19) and
537 Commentary, American Concrete Institute, Detroit, USA, 2019.
- 538 [26] FIB, Fib Model Code for Concrete Structures 2010, Fédération Internationale du Béton, Ernst &
539 Sohn, Berlin, Germany, 2013.
- 540 [27] L.H. Han, G.H. Yao, Z. Tao. Performance of concrete-filled thin-walled steel tubes under pure
541 torsion, *Thin-Walled Struct.* 45(1) (2007) 24-36.
- 542 [28] Z. Tao, Z.B. Wang, Q. Yu, Finite element modelling of concrete-filled steel stub columns under
543 axial compression, *J. Constr. Steel. Res.* 89 (2013) 121-131.
- 544

Figures:

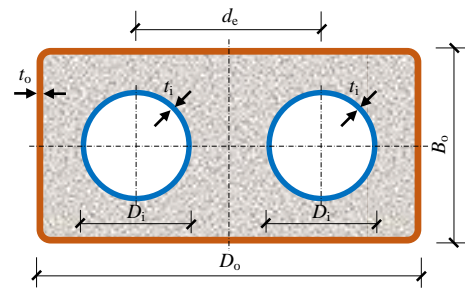
(a) With double steel SHSs

(b) With double steel CHSs

Fig. 1. Typical configuration of rectangular DCFSSST members.



(a) Section with double steel SHSs



(b) Section with double steel CHSs

Fig. 2. Cross-sectional dimensions of the specimens.

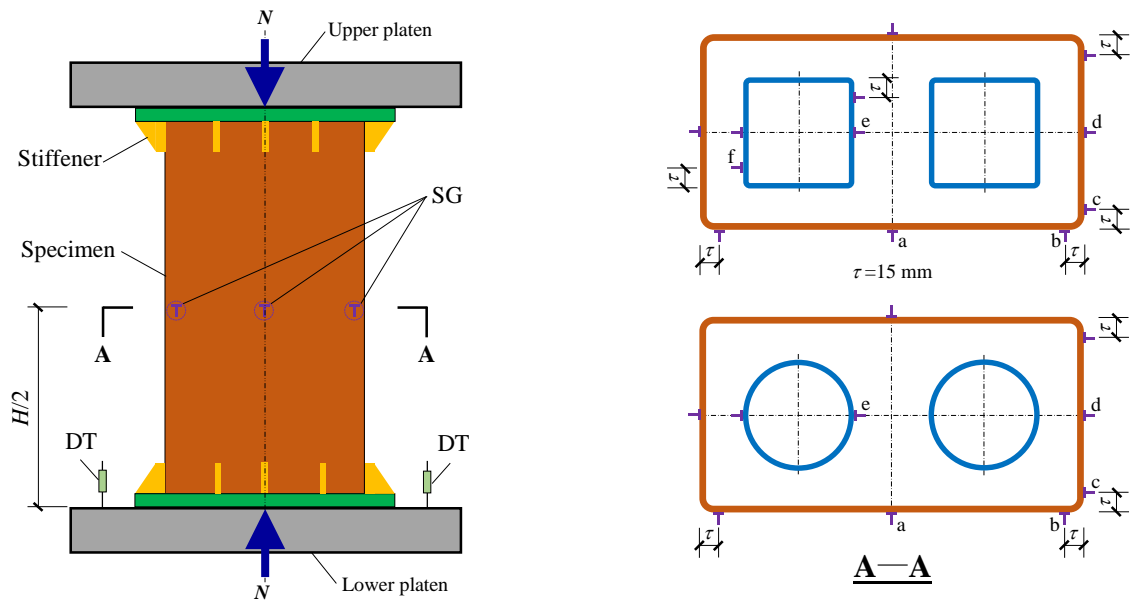
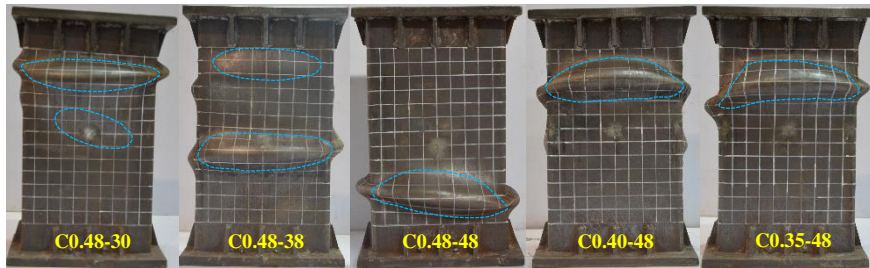


Fig. 3. Test set-up and measuring point arrangement.



(a) With double steel SHSs



(a) With double steel CHSs

Fig. 4. Overall failure mode of the specimens.



(a) With double steel SHSs



(b) With double steel CHSs

Fig. 5. Failure mode of the sandwiched concrete.

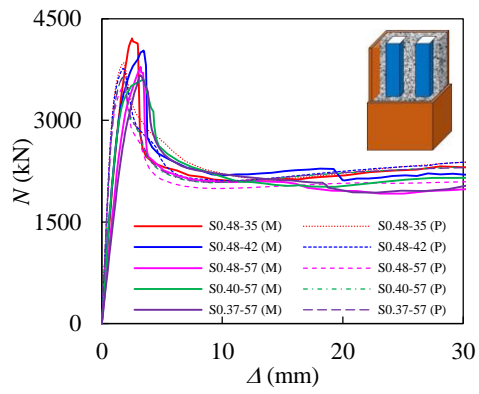


(a) With double steel SHSs

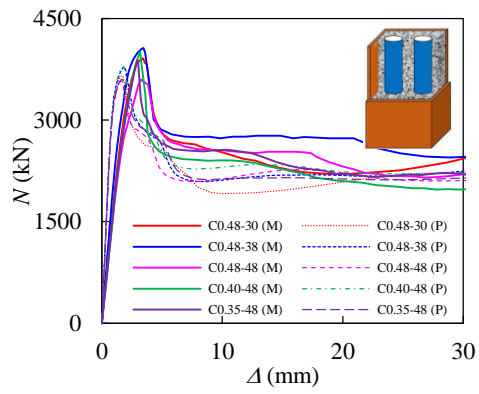


(b) With double steel CHSs

Fig. 6. Failure mode of inner tubes.

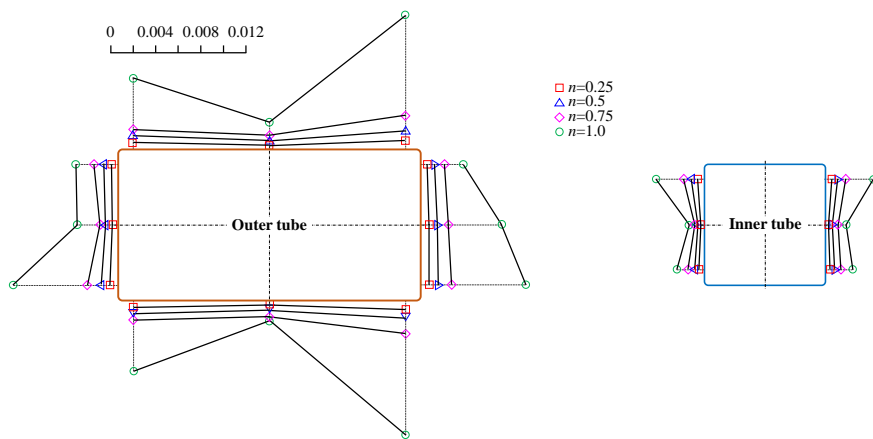


(a) With double steel SHSs

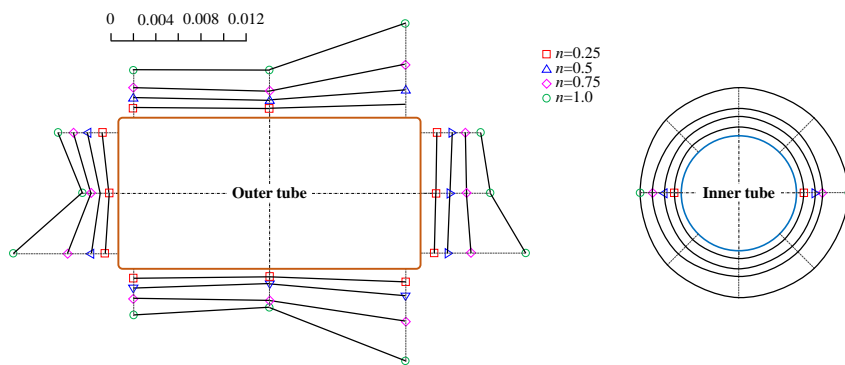


(b) With double steel CHSs

Fig. 7. Load (N) versus axial displacement (Δ) curve of the specimens.

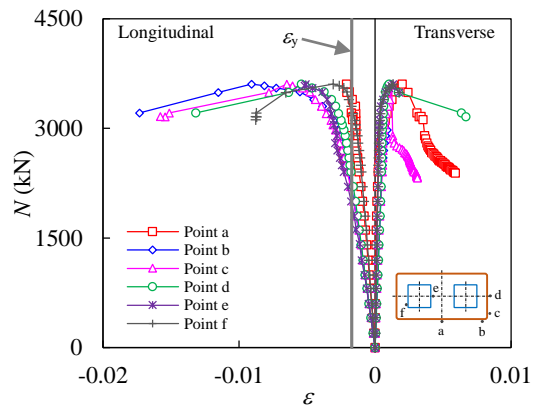


(a) S0.40-57

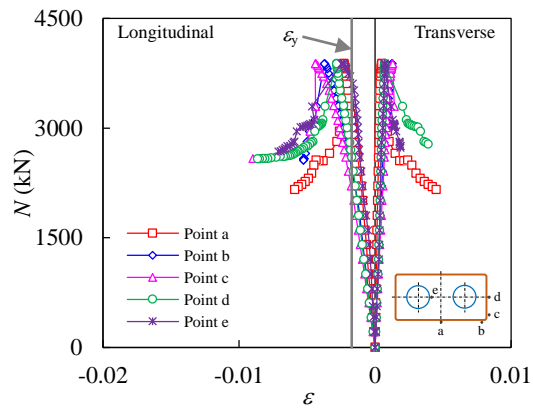


(b) C0.35-48

Fig. 8. Typical longitudinal strain distribution during the loading process.

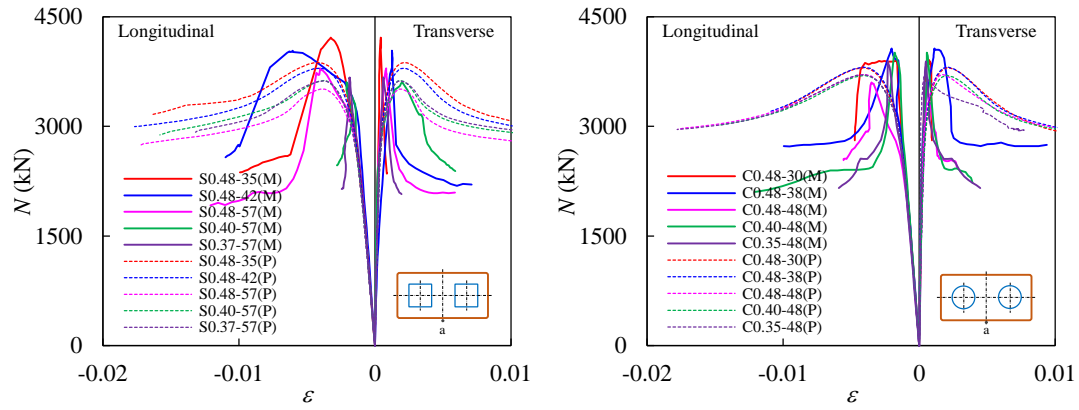


(a) S0.40-57

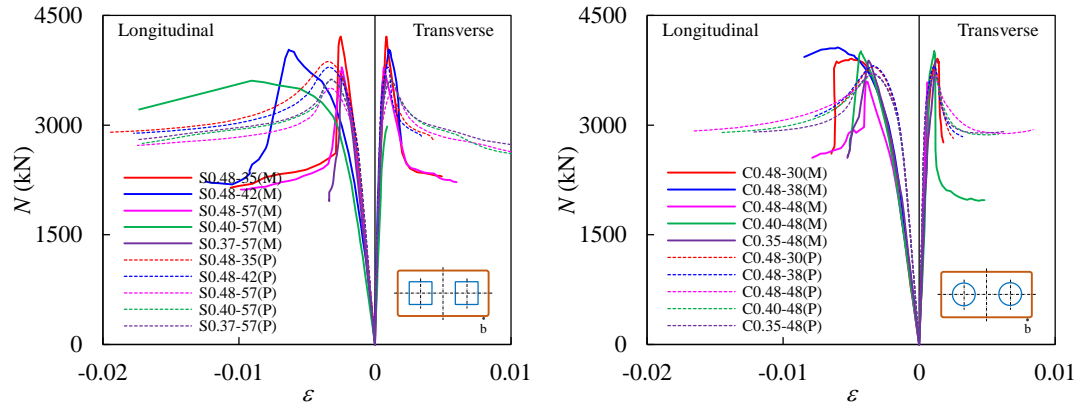


(b) C0.35-48

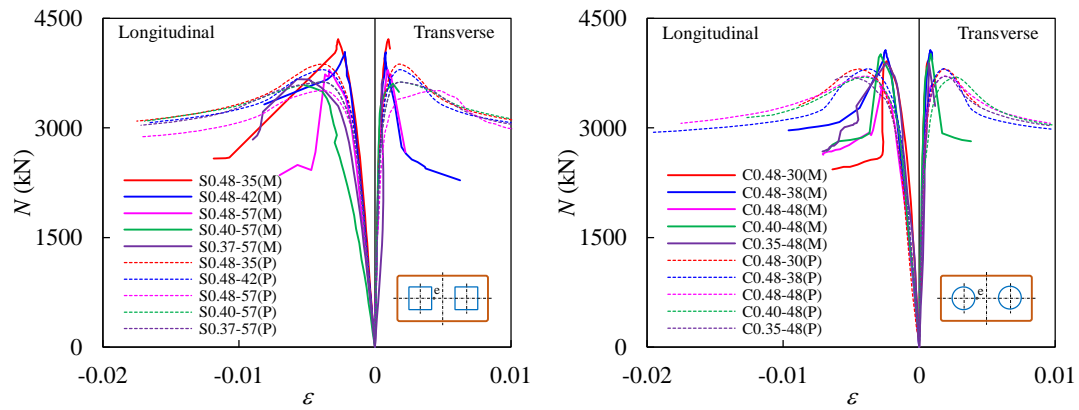
Fig. 9. Load versus strain curves of typical specimens.



(a) Point a

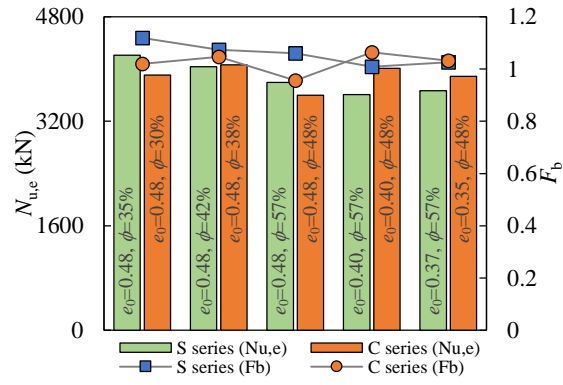


(b) Point b

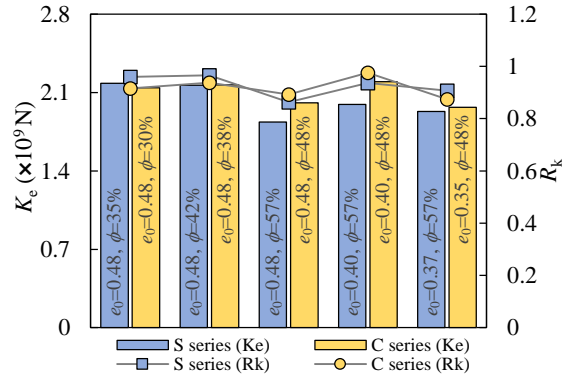


(c) Point e

Fig. 10. Effect of parameters on $N - \varepsilon_L$ curves at representative points.



(a) $N_{u,e}$ and F_b



(b) K_e and R_k

Fig. 11. Effect of parameters on $N_{u,e}(F_b)$ and $K_e(R_k)$

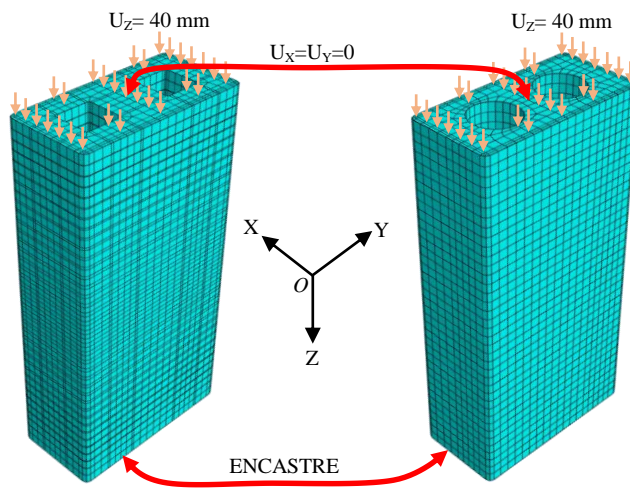
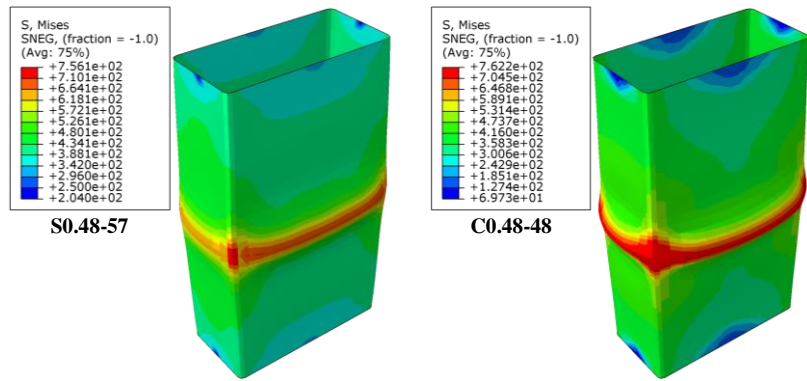
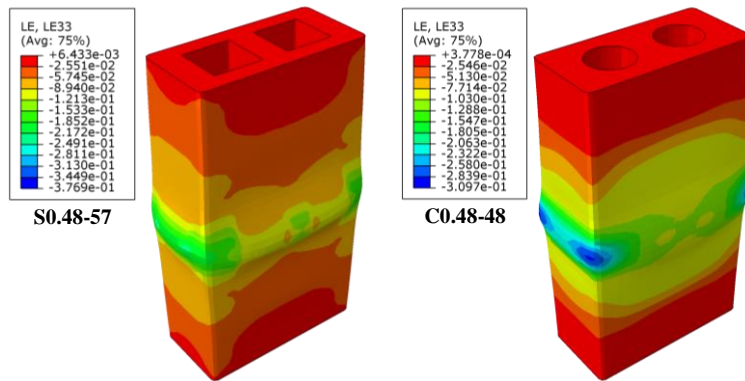


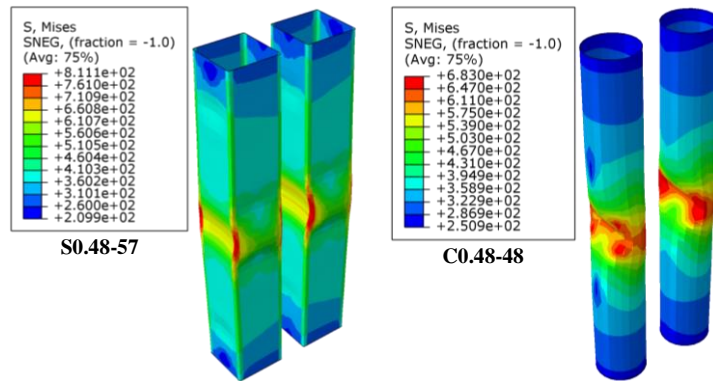
Fig. 12. Meshing and boundary conditions.



(a) Outer tube



(b) The sandwiched concrete



(c) Inner tubes

Fig. 13. The simulated failure mode of different components in typical specimens.

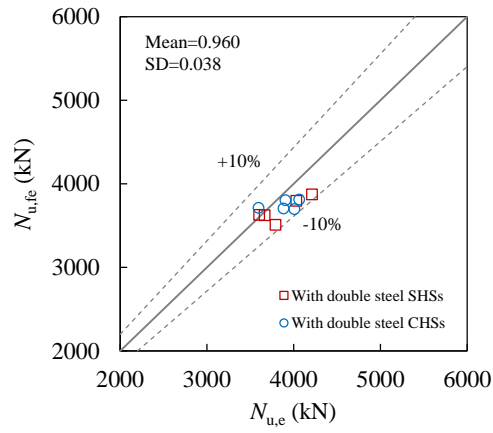
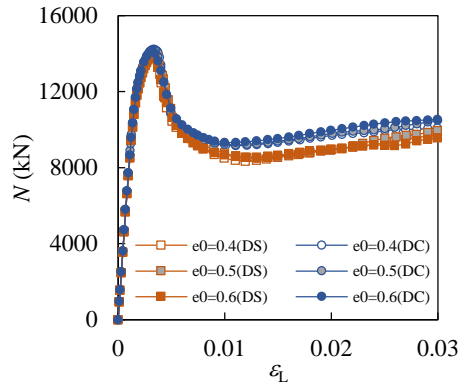
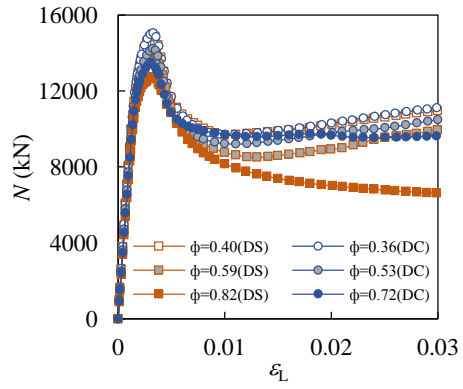


Fig. 14. Comparison between the simulated and measured bearing capacities.

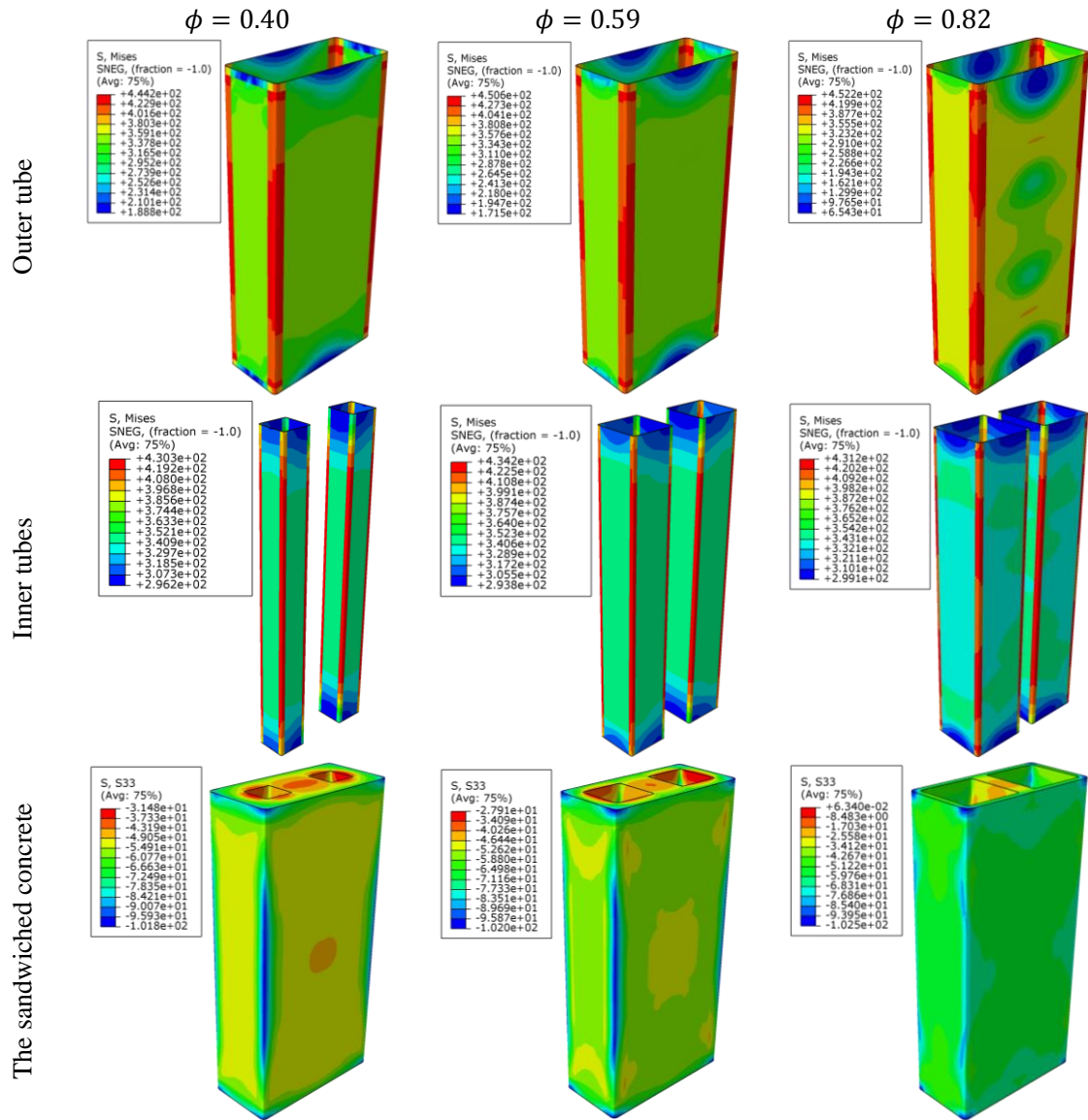


(a) Variation in e_0

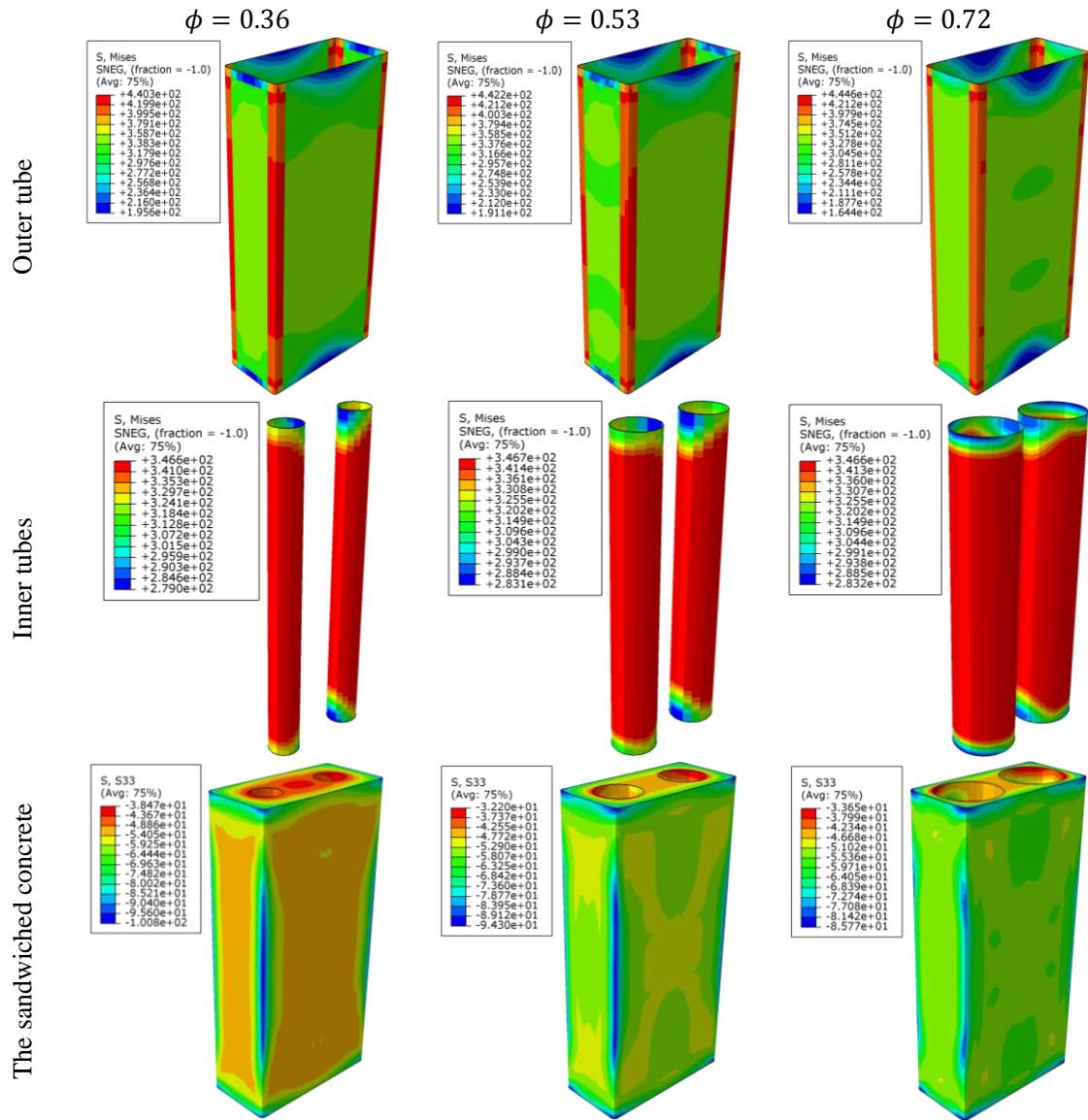


(b) Variation in ϕ

Fig. 15. $N - \varepsilon_L$ curve of typical rectangular DCFSSST stub columns under axial compression.

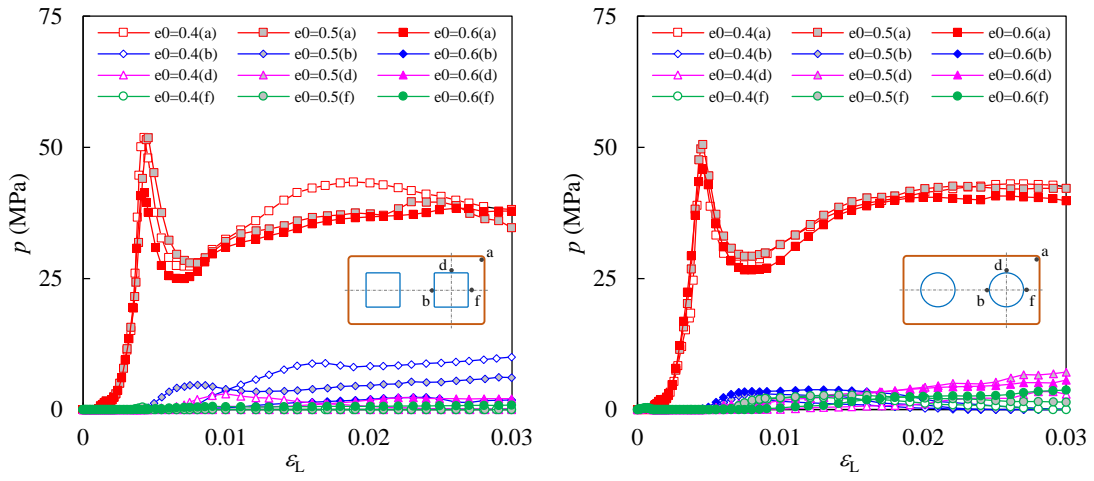


(a) Columns with double steel SHSs

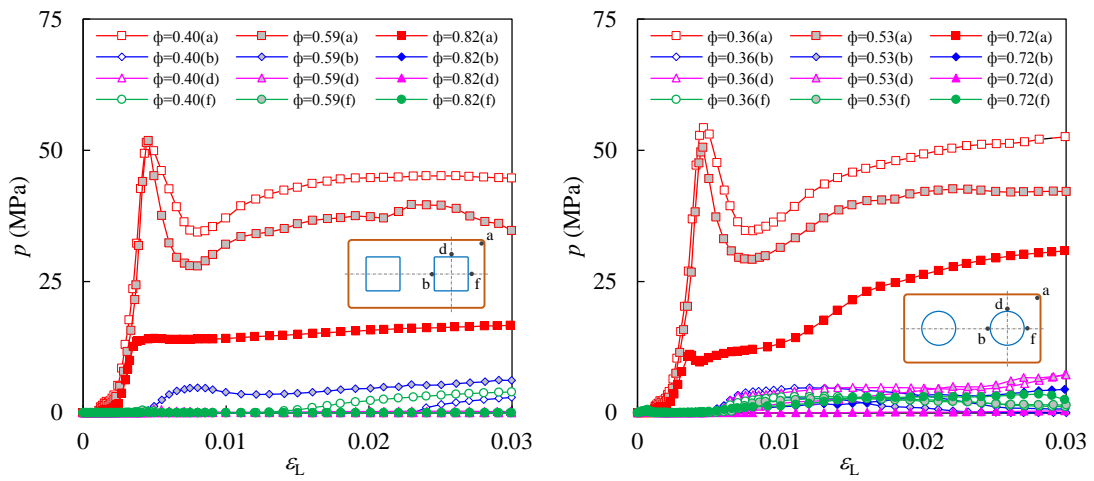


(b) Columns with double steel CHSs

Fig. 16. Effect of ϕ on stress state of different components in the axially compressed rectangular DCFSSST stub columns while reaching the bearing capacity.

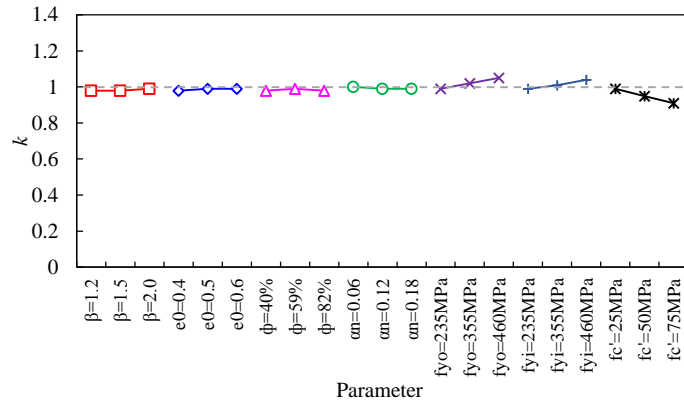


(a) Variation in e_0

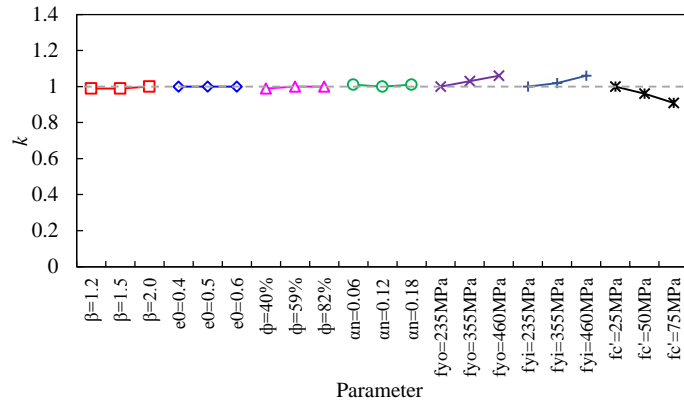


(b) Variation in ϕ

Fig. 17. Effect of e_0 and ϕ on interaction stress between steel tube and concrete.



(a) With double steel SHSs



(b) With double steel CHSs

Fig. 18. Effect of parameters on the strength index ratio (k)

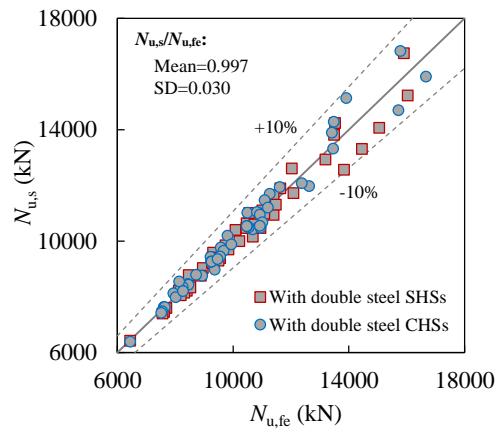


Fig. 19. Comparison between the simplified and numerical bearing capacities.

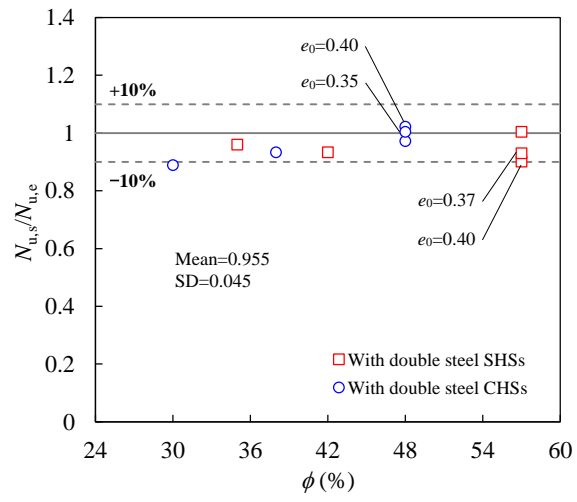


Fig. 20. Comparison between the simplified and measured bearing capacities.

Tables:**Table 1.** Information of the test specimens.

No.	Label	$D_o \times B_o \times t_o$ (mm)	D_o/t_o	$D_i \times t_i$ (mm)	D_i/t_i	d_e (mm)	e_0	ϕ	$N_{u,e}$ (kN)	$N_{u,fe}$ (kN)	$N_{u,fe}/N_{u,e}$	K_e ($\times 10^9$ N)
1	S0.48-35	300×150×5.65	53.1	50×2.55	19.6	144	0.48	35%	4214	3873	0.919	2.18
2	S0.48-42	300×150×5.65	53.1	60×2.54	23.6	144	0.48	42%	4034	3796	0.941	2.16
3	S0.48-57	300×150×5.65	53.1	80×2.51	31.9	144	0.48	57%	3793	3509	0.925	1.84
4	S0.40-57	300×150×5.65	53.1	80×2.51	31.9	120	0.40	57%	3607	3628	1.006	1.99
5	S0.37-57	300×150×5.65	53.1	80×2.51	31.9	110	0.37	57%	3669	3625	0.988	1.93
6	C0.48-30	300×150×5.65	53.1	48×3.55	13.5	144	0.48	30%	3910	3805	0.973	2.14
7	C0.48-38	300×150×5.65	53.1	60×3.55	16.9	144	0.48	38%	4065	3812	0.938	2.17
8	C0.48-48	300×150×5.65	53.1	76×3.54	21.5	144	0.48	48%	3600	3712	1.031	2.01
9	C0.40-48	300×150×5.65	53.1	76×3.54	21.5	120	0.40	48%	4010	3698	0.922	2.20
10	C0.35-48	300×150×5.65	53.1	76×3.54	21.5	106	0.35	48%	3886	3706	0.954	1.97

Table 2. Properties of steel sections.

Type	Cross-section	$D_o(D_i) \times t_o(t_i)$ (mm×mm)	f_y (MPa)	f_u (MPa)	E_s (N/mm ²)	μ_s	δ (%)
Outer tube	Rectangular	300×5.65	346.5	527.5	2.03×10^5	0.273	30.0
		50×2.55	272.8	356.4	1.88×10^5	0.242	15.8
Inner tube	Square	60×2.54	315.3	407.6	1.85×10^5	0.290	14.3
		80×2.51	303.5	406.2	1.80×10^5	0.268	17.8
	Circular	48×3.55	265.2	348.2	1.99×10^5	0.334	16.0
		60×3.55	329.8	383.4	1.87×10^5	0.277	24.0
		76×3.54	293.6	432.7	1.74×10^5	0.266	28.3

Table 3. Mix proportion and properties of concrete.

Mix proportion (kg/m ³)						Properties				
Cement	Fly ash	Sand	Coarse aggregate	Tap water	Water reducer	$f_{cu,28}$ (MPa)	f_{cu} (MPa)	E_c (GPa)	Slump (mm)	Spread (mm)
420	130	800	832	196	5.32	49.4	61.3	31.6	270	600